# Flow Visualization in a Linear Turbine Cascade of High Performance Turbine Blades

H. P. Wang

S. J. Olson

R. J. Goldstein

E. R. G. Eckert

Department of Mechanical Engineering, University of Minnesota, Minneapolis, MN 55455 Multiple smoke wires are used to investigate the secondary flow near the endwall of a plane cascade with blade shapes used in high-performance turbine stages. The wires are positioned parallel to the endwall and ahead of the cascade, within and outside the endwall boundary layer. The traces of the smoke generated by the wires are visualized with a laser light sheet illuminating various cross sections around the cascade. During the experiment, a periodically fluctuating horseshoe vortex system of varying number of vortices is observed near the leading edge of the cascade. A series of photographs and video tapes was taken in the cascade to trace these vortices. The development and evolution of the horseshoe vortex and the passage vortex are clearly resolved in the photographs. The interation between the suction side leg of the horseshoe vortex and the passage vortex is also observed in the experiment. A vortex induced by the passage vortex, starting about one-fourth of the curvilinear distance along the blade on the suction surface, is also found. This vortex stays close to the suction surface and above the passage vortex in the laminar flow region on the blade. From this flow visualization, a model describing the secondary flows in a cascade is proposed and compared with previous published models. Some naphthalene mass transfer results from a blade near an endwall are cited and compared with the current model. The flows inferred from the two techniques are in good agreement,

#### Introduction

The secondary flow in a turbine cascade is of interest to both designers and researchers. Current design methods for a turbine blade passage are usually based on two-dimensional flow analysis. However, close to the endwall, flow separation, a horseshoe vortex, a passage vortex, and some small but very intense corner vortices at the junction of the endwall and blade may affect the aerodynamic performance of a turbine and increase the heat transfer from the hot fluid to the blade and endwall surfaces. A comprehensive review of the secondary flow structures in turbine cascades has been presented by Sieverding (1985). Detailed experimental information about secondary flow visualization and the secondary flow patterns can be found in the studies by Jabbari et al. (1992), Langston (1990), Yamamoto (1987a, 1987b), Sonoda (1985), Langston et al. (1977), Marchal and Sieverding (1977), and Chung and Simon (1990), to name just a few.

Several secondary flow models have been published to assist in visualizing the flow patterns and to aid in understanding this complicated flow. Three representative models of the flow pattern, found in the literature, are shown in Fig. 1. Figure 1(a) (Langston, 1980) shows a general picture of the evolution and development of two legs of a horseshoe vortex and a passage vortex. The second flow pattern, given by Sharma and Butler (1987) and shown in Fig. 1(b), demonstrates that the suction leg wraps itself around the passage vortex instead of adhering to the suction side. The third model, shown in Fig. 1(c), is presented by Goldstein and Spores (1988). Based on mass transfer results, they proposed that the suction leg of the horseshoe vortex stays above the passage vortex and travels with it. The location of the suction leg of the horseshoe vortex is the major difference among the three models. It is difficult to follow

Contributed by the International Gas Turbine Institute and presented at the 40th International Gas Turbine and Aeroengine Congress and Exhibition, Houston, Texas, June 5–8, 1995. Manuscript received by the International Gas Turbine Institute February 4, 1995. Paper No. 95-GT-7. Associate Technical Editor: C. J. Russo.

the suction leg as it moves down the passage. Most pressure or velocity maps in the literature do not give a clear picture of how this leg develops. Its small size combined with a strong stretching in the streamwise direction makes it difficult to detect. Moore and Smith (1984) detected ethylene around the passage vortex core at the exit of a cascade when ethylene was injected at the leading edge suction side. The suction leg appears almost completely mixed with the passage vortex, at least in the exit plane. A similar phenomenon was also observed by Sieverding and Van den Bosche (1983) with their colored-smoke visualization. They found that the suction side leg wraps around the passage vortex. The flow pattern suggested by Jilek (1986) is similar to that in Fig. 1(c).

Jabbari et al. (1992) presented a set of oil-lampblack flow visualization photographs on an endwall and blade suction surfaces, which were compared with local mass transfer results. They observed a suction corner vortex in the middle of the passage climbing up and adhering to the suction surface until far downstream. This vortex was also observed by Sonoda (1985) in his kerosene vapor flow visualization.

The present study uses a multiple smoke-wire flow-visualization technique to observe and trace the vortices of interest and compares the flow pattern with results of local mass transfer measurements. A series of photographs and videos have been taken for archival use. Based on the flow visualization results, a new model is presented to better understand the secondary flow

# Experimental Apparatus

Wind Tunnel and Linear Cascade. An open circuit, blower-type wind tunnel is used in these investigations. A 22.4 kW blower is used to drive the flow through a honeycomb flow straightener and three graduated, high-porosity screens before contracting the flow in a 6.25:1 area-ratio contraction. The flow leaves the contraction and enters the test facility, which has a 45.7 cm by 45.7 cm cross section.

A facility for flow visualization and experimental mass transfer tests on gas turbine airfoils and passages has recently been

built. The test facility following the contraction exit, is shown in a scaled drawing from above in Fig. 2. It is a four-blade, linear cascade, with a high-performance blade profile. Figure 2 also shows two interchangeable sections upstream of the cascade: a straight duct and a grid duct section. The grid duct section has two slots to accommodate turbulence generating grids, but none were used in these investigations. The flow is tripped at the contraction exit, however, to disturb the boundary layer approaching the cascade.

The blade nomenclature is shown in Fig. 3 and the cascade geometry data are given in Table 1. A modern, high-performance blade profile is used in these investigations. The blade profile is specified in Table 2. For these tests, it was necessary to use low-speed flow in order to photograph the smoke traces clearly. A Reynolds number based on the exit velocity and blade chord length of  $2.7 \times 10^4$  gave good flow visualization results. The undisturbed flow entering the facility from the contraction is highly uniform with a free-stream turbulence intensity less than 0.2 percent, measured at the contraction exit.

Two tail boards trailing the outermost blades, and two flexible bleeds outside the outermost blades, are used to adjust the flow within the three turbine passages. The flow is balanced by comparing pressure measurements, made while using a special pressure measurement blade, on the surfaces of Blades 2 and 3 with each other and with a potential flow calculation. The pressure distribution along the blades is quite sensitive to these adjustments, but good agreement between the blades and the analytical prediction could be achieved. An example of the pressure distribution on the two inner blades is shown in Fig. 4. In addition, measurements of the flow velocity at the midspan of the tunnel show that the flow, measured at the measurement slot shown in Fig. 2 nearest the cascade, varies by less than 2 percent in the cross-stream direction when the tunnel has been balanced using these adjustments.

Flow Visualization. The test section side walls are Plexiglas, which allows unobstructed observation of the flow within the cascade. An extensive smoke-wire flow visualization study has been conducted and video taped with the aid of a laser light sheet. Eight 0.102 mm 304 stainless steel wires were positioned parallel to the endwall ahead of the cascade. The distances from the eight wires to the endwall are 3.2, 6.4, 12.7, 19.1, 25.4, 31.8, 38.1, and 50.8 mm respectively.

A thin layer of light-duty machine oil was applied to the wires, which were electrically heated to produce smoke. A glass rod was used to expand the beam from a He-Ne laser into a sheet to illuminate cross-sectional slices of the flow, made visible by the smoke generation. The smoke traces produced are distinct and can be identified individually as the flow develops in the blade passage.

Photographs of the visualized flow patterns were made using a Nikon N8008s camera with a 1:2.8 105 mm AF Micro Nikkor Lens using Kodak Tmax 3200P film pushed to 6400 speed and shot with an aperture of f2.8 and shutter speed of  $\frac{1}{30}$  or  $\frac{1}{60}$ th of

a second. Four sets of video tape have also been produced that follow the vortex flow pattern from different view angles.

#### **Results and Discussion**

Inlet Flow Description. Velocity measurements were made to characterize the flow approaching the cascade and to provide some insight into the flow patterns that were observed. Measurements were made using a TSI IFA-100 hot-wire anemometer with a 1218-T1.5 single-wire boundary-layer probe. The flow approaching the cascade was measured at a location 77 cm from the contraction exit, shown as point B in Fig. 2. The mean flow velocity was 0.8 m/s with a turbulence intensity less than 0.2 percent, which gives a Reynolds number based on the blade chord length and exit velocity of  $2.7 \times 10^4$ . The low velocity was necessary to obtain clear flow visualization photographs. At this condition, the displacement thickness was measured to be 4.9 mm and the boundary layer shape factor was found to be 2.48. Due to the low velocity required for flow visualization, the inlet boundary layer remains laminar despite the trip used at the contraction exit.

The flow visualization results to be presented were obtained at these conditions. Typical flow conditions entering the blade section of a real engine are characterized by high turbulence levels, large length scales, and exit Reynolds numbers on the order of 20 to 50 times higher than that used for these flow visualization studies. Additional tests were conducted with higher velocities to produce a turbulent boundary layer at the cascade inlet. The results show a flow pattern similar to that of a laminar inlet boundary layer condition; however, due to the higher velocities, the photographic results were rather poor. In addition, surface flow visualization results at typical engine Reynolds numbers have been conducted with variations in the free-stream turbulence level generated by grids. The flow patterns we infer from the visualizations look similar to one another, although the path and size of the passage vortex are affected by the turbulence level. Other testing is currently under way to examine the effect of turbulence length scale as well. From these additional tests, we conclude that the general flow pattern, described below, is similar to that which would be found at engine conditions.

Flow Visualization. Figures 5–7 contain photographs of the smoke wire patterns. The position of the laser light sheet is indicated by the dashed lines in the left row of the figures and the position of the camera is also indicated.

It was observed in the smoke visualization that the flow exhibits fluctuations in the inlet region of the channel with a frequency of approximately 2.5 Hz. The effect of this on the vortex development is shown in Fig. 5, where sequences of photographs taken at approximately 3.2 frames per second are shown. In this figure, three light sheet positions are shown, with a time sequence of four photographs following them. In Figs. 6 and 7, the positions of the light sheet and camera change in each photograph.

### - Nomenclature -

b = axial chord length of blade

c =chord length of blade

 $C_{Ps}$  = static pressure coefficient =  $(P_s - P_{s0})/(\rho U_{in}^2/2)$ 

l =blade span (length between endwalls)

p = pitch length of blades

 $\hat{P}_s = \text{local static pressure}$ 

 $P_{s0}$  = upstream reference static pressure (point A in Fig. 2)

 $Re_{ex}$  = exit Reynolds number =  $\rho U_{ex} c/\mu$ 

 $S_s$  = curvilinear (streamwise) coordinate along suction side;  $S_s$  = 0 at stagnation line

t = time

 $t_0$  = reference time for time series photographs

 $U_{in}$  = incoming velocity (measured at point B in Fig. 2)

 $U_{ex}$  = exit velocity (calculated from incoming velocity and cascade geometry)

V = vortex label, defined in Fig. 8

x = coordinate in axial chord direction, defined in Fig. 3

y = coordinate normal to the axial chord, defined in Fig. 3

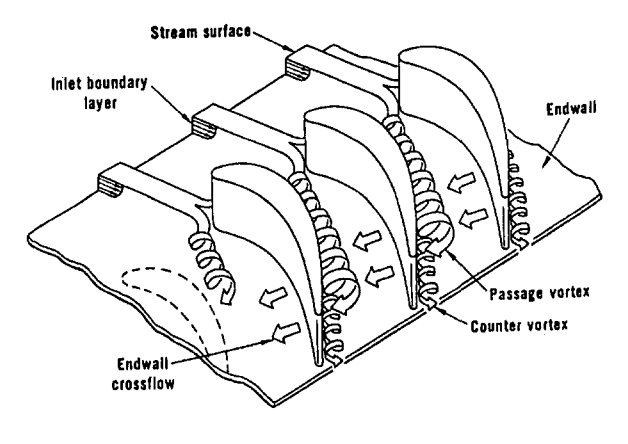
z = spanwise coordinate of blade starting from endwall

 $\beta_1$  = blade inlet angle = 35 deg

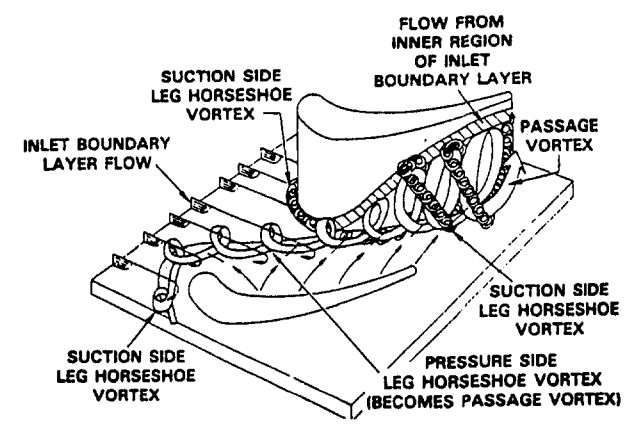
 $\beta_2$  = blade outlet angle = -72.49 deg

 $\mu$  = dynamic viscosity of air

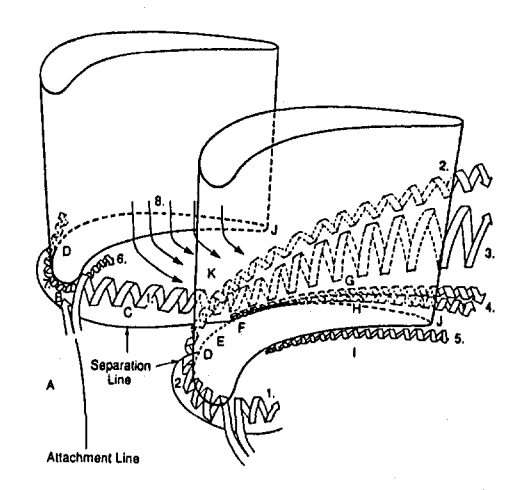
 $\rho$  = density of air



(a) Vortex pattern described by Langston (1980).



(b) Vortex pattern described by Sharma and Butler (1987).



(c) Vortex pattern described by Goldstein and Spores (1988).

Fig. 1 Vortex patterns described in the literature

A perspective view of the secondary flow pattern based on the smoke patterns in Figs. 5–7 and the previous observations of Goldstein and Spores (1988) and Jabbari et al. (1992) is shown in Fig. 8. It should be pointed out that the tightness of the spirals representing the vortices in the picture have been chosen for clarity of the presentation. In reality, the passage vortex, for example, was found to turn much less tightly (Sieverding and Van den Bosche, 1983; Sonoda, 1985; Chung and Simon, 1990). Our observation is that the passage vortex makes approximately one and one half rotations as it passes

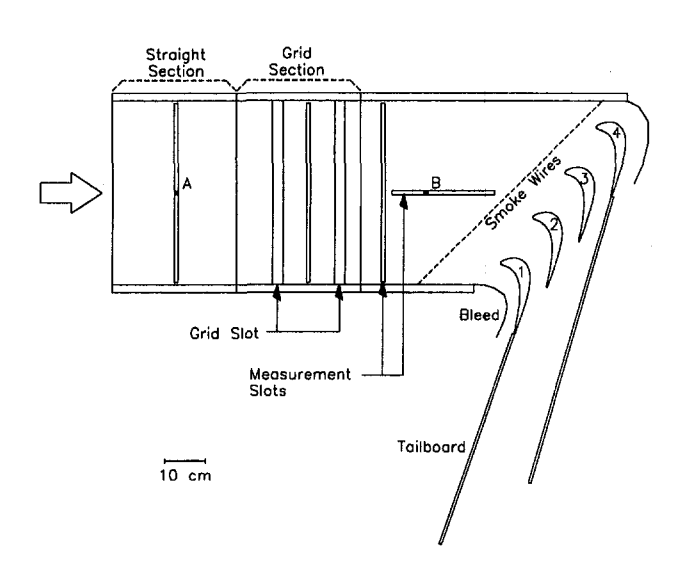


Fig. 2 Turbine cascade viewed from above

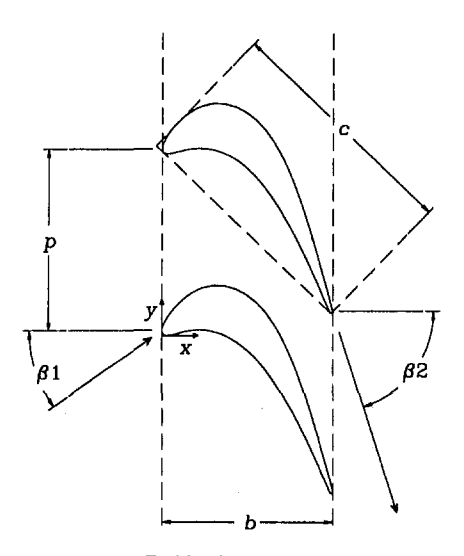


Fig. 3 Turbine blade arrangement

Table 1 Cascade geometry data

Number of blades	4
Chord length of blade - c	184.15 mm
Axial Chord to Chord ratio - $b/c$	0.704
Pitch to Chord ratio - $p/c$	0.750
Aspect ratio (Span/Chord) - $l/c$	2.483
Blade inlet angle - $\beta_1$	35°
Blade outlet angle - $\beta_2$	72.49°
Incoming Velocity - Uin	0.80 m/s
Exit Velocity - Uex	2.18 m/s
Reynolds Number - Reex	$2.7 \times 10^4$
(for all flow visualization)	

through the cascade. An interpretation of the results will now be presented.

Stagnation Point Flow. The development of a horseshoe vortex at the stagnation line of a cylinder near an endwall depends on the approaching boundary layer and on the boundary layer forming around the cylinder. In previous studies of flow around a cylinder, the cylinder radius was generally larger than the thickness of the approaching boundary layer. A relatively

Table 2 Turbine blade geometry

x/b	y/b	x/b	y/b	x/b	y/b
0.0000	0.0242	0.2365	0.2752	0.7735	-0.1793
0.0014	0.0377	0.2989	0.2886	0.8071	-0.2703
0.0063	0.0550	0.3656	0.2868	0.8383	-0.3621
0.0155	0.0759	0.4328	0.2684	0.8678	-0.4545
0.0296	0.1001	0.4967	0.2348	0.8959	-0.5473
0.0484	0.1269	0.5556	0.1878	0.9229	-0.6404
0.0722	0.1565	0.6083	0.1304	0.9491	-0.7338
0.1014	0.1878	0.6552	0.0646	0.9747	-0.8273
0.1376	0.2200	0.6942	-0.0025	0.9997	-0.9210
0.1822	0.2506	0.7364	-0.0897	1.0000	-0.9235
0.0000	0.0242	0.1147	0.0124	0.7238	-0.3864
0.0009	0.0146	0.1434	0.0190	0.7603	-0.4519
0.0031	0.0079	0.1760	0.0244	0.7950	-0.5183
0.0052	0.0038	0.2133	0.0273	0.8282	-0.5854
0.0070	0.0013	0.2551	0.0256	0.8603	-0.6531
0.0085	0.0000	0.3006	0.0180	0.8914	-0.7212
0.0098	-0.0007	0.3478	0.0035	0.9218	-0.7897
0.0120	-0.0018	0.3950	-0.0175	0.9515	-0.8585
0.0153	-0.0031	0.4412	-0.0452	0.9807	-0.9274
0.0205	-0.0046	0.4857	-0.0789	0.9828	-0.9306
0.0279	-0.0055	0.5286	-0.1184	0.9859	-0.9327
0.0384	-0.0054	0.5695	-0.1626	0.9895	-0.9336
0.0522	-0.0035	0.6088	-0.2112	0.9932	-0.9330
0.0694	0.0003	0.6441	-0.2596	0.9968	-0.9309
0.0903	0.0058	0.6853	-0.3222	0.9992	-0.9276
				1.0000	-0.9235

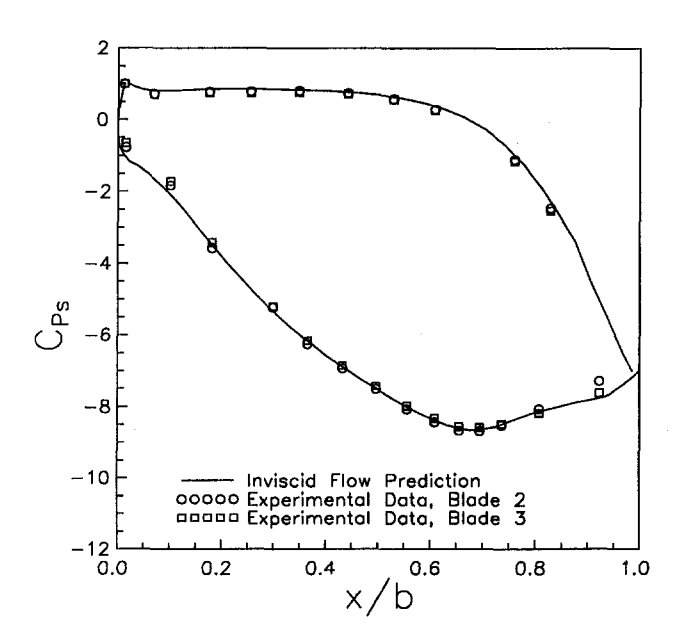


Fig. 4  $\,$  Pressure coefficient along the surfaces of blades 2 and 3 for  $Re_{ex} = 5.4 \times 10^5$ 

large vortex developed near the corner with smaller vortices close by.

The present high-performance blade has a small radius of curvature, approximately equal in size to the approaching boundary layer thickness. Figure 5 shows that the corner flow near the stagnation line develops two vortices of about equal

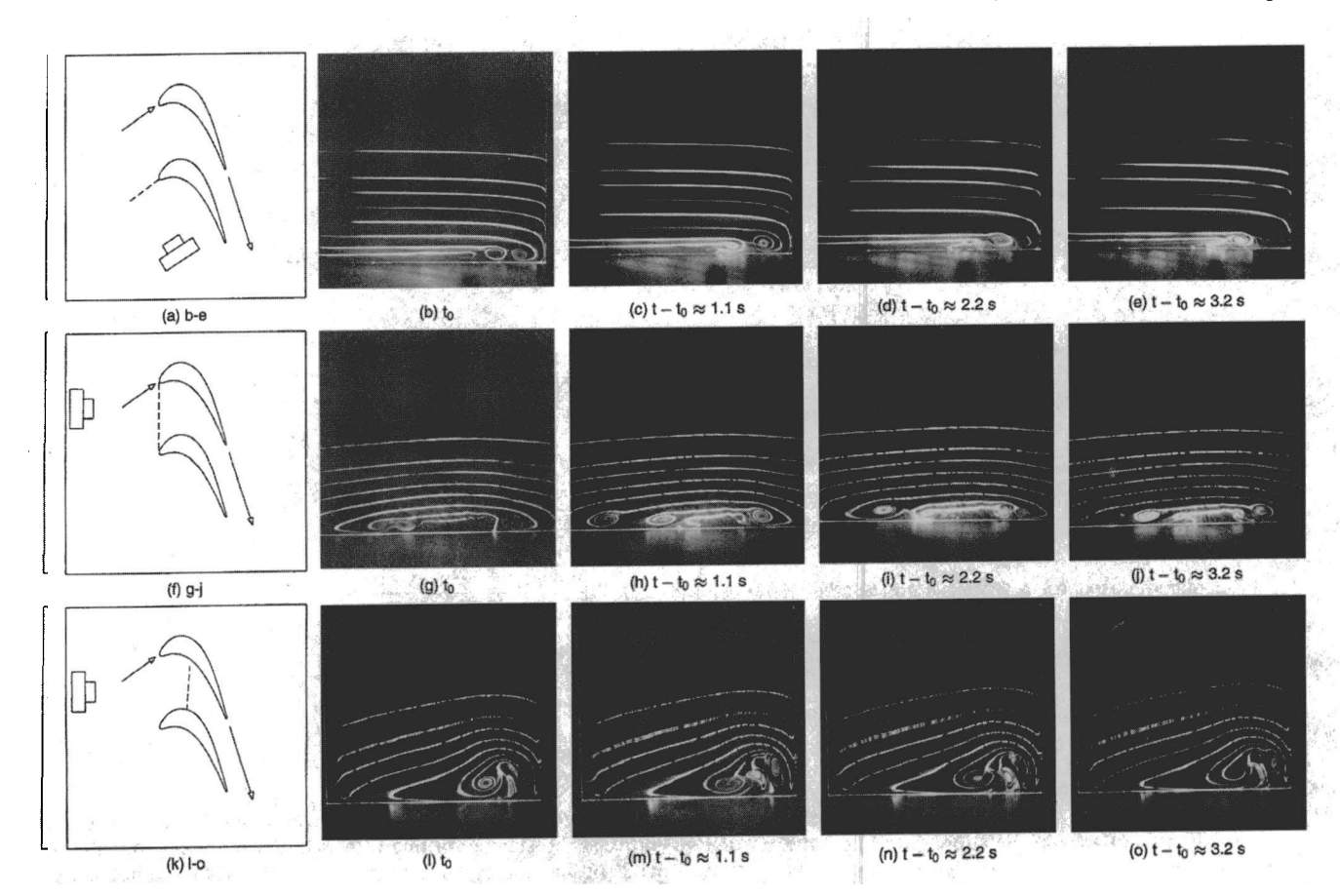


Fig. 5 Leading edge and entrance flow visualization (time series photographs)

sizes at different distances from the blade surface. The fluctuations of flow near the vortices described before causes the arrangement of the vortices to change periodically, as shown in the sequence of photographs in Figs. 5(b-e). The photographs are taken at approximately 3.2 frames per second. The frequency of the vortex movement is about 2.5 Hz. Although the photographs do not follow the motion in one period, they do demonstrate the periodicity of the multivortex structure with varying numbers formed ahead of the blade. Section A-A in Fig. 8 shows two forms that the pressure side leg of the passage vortex takes as it changes periodically.

When the vortices enter the passage, the multi-vortex structure is gradually changed to a single-vortex pattern. It is essentially diminished at the point where the pressure side leg of the horseshoe vortex meets its counterpart from the suction side. The vortices continue to oscillate as they move downstream.

Figures 6 and 7 show slices of the flow in the passage at many locations. It is clear that the major part of the secondary flow is the passage vortex. It is responsible for much of the pressure loss across the cascade and high heat transfer to the blade and endwall. The others involved are the horseshoe vortex pair, and a new counter-rotating wall vortex induced by the passage vortex.

Pressure Side Leg of the Horseshoe Vortex,  $V_{ph}$ . It is seen in Figs. 6(f)-(h) and (j)-(l), and depicted in Fig. 8, that due to a strong pressure gradient, the pressure leg of the horse-

shoe vortex immediately moves toward the suction side after it enters the passage. It entrains the main flow and the inlet boundary layer. This multi-vortex leg is gradually squeezed into a single vortex (Figs. 6(o) - (p)) as it approaches the point where its counterpart, the suction leg from the adjacent blade, joins. This location occurs at approximately 1/4 of the surface distance from the blade leading edge. Goldstein et al. (1995) measured mass transfer on the suction surface of a turbine blade. They found that the maximum mass transfer rate occurs around this location for the case when only the blade is an active mass transfer surface. A contour plot of their naphthalene mass transfer results, Fig. 9, on part of the suction surface is shown here for comparison. Even though the blade geometry used in that study is different from the current one, the basic structure of the secondary flow is expected to be similar. It should be noted that while the flow pattern will be unchanged when the endwall is also an active mass transfer surface, the mass transfer coefficient will be diminished in this area, since the vortex flow is composed primarily of boundary layer fluid.

At the two-leg merging point, the interaction among different flow components, such as the counter-rotating horseshoe legs, the incoming boundary layer, the endwall crossflow, and the mainstream, form an even stronger vortex in the passage, which is called the passage vortex. Since the pressure leg has the same sense of rotation as the passage vortex, Langston (1980) credited this pressure leg as part of the passage vortex.

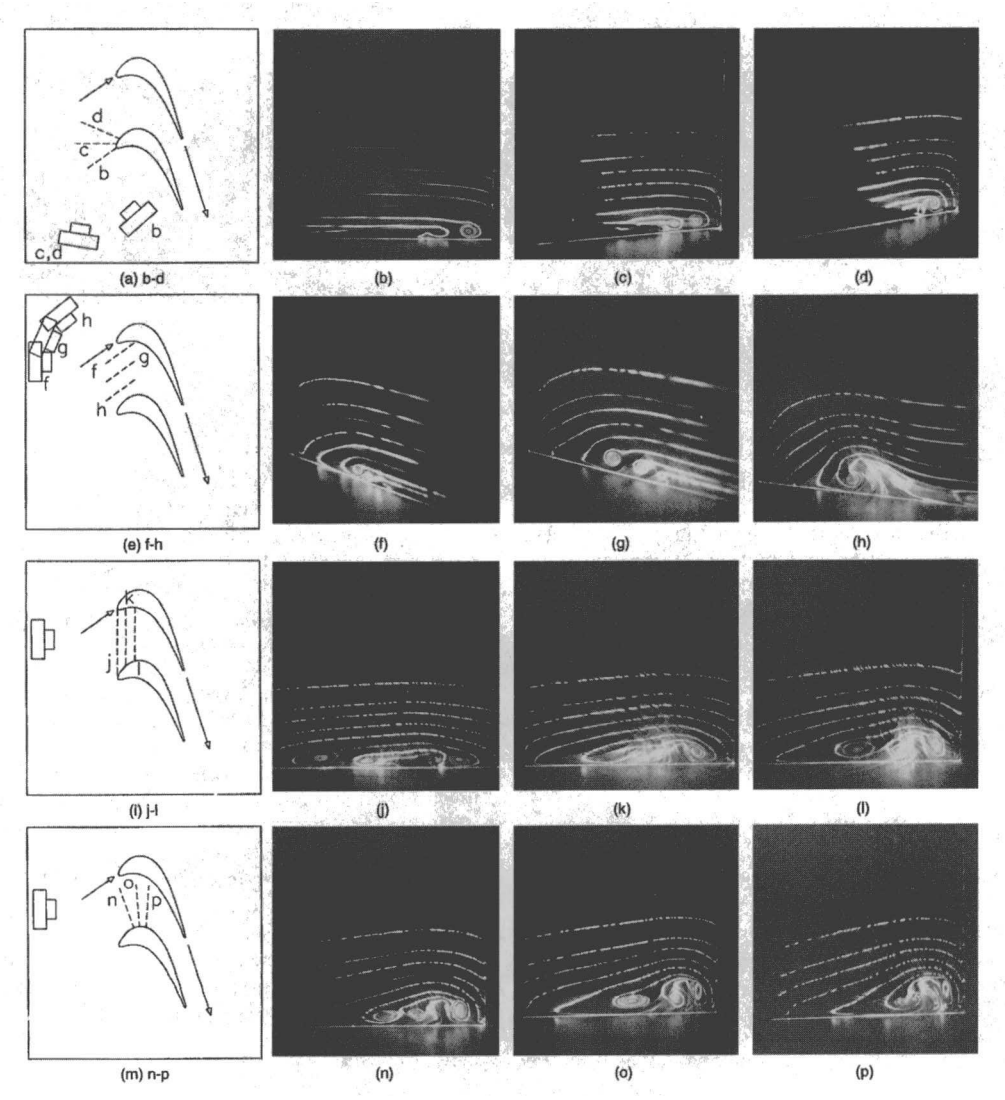


Fig. 6 Flow visualization around the blades

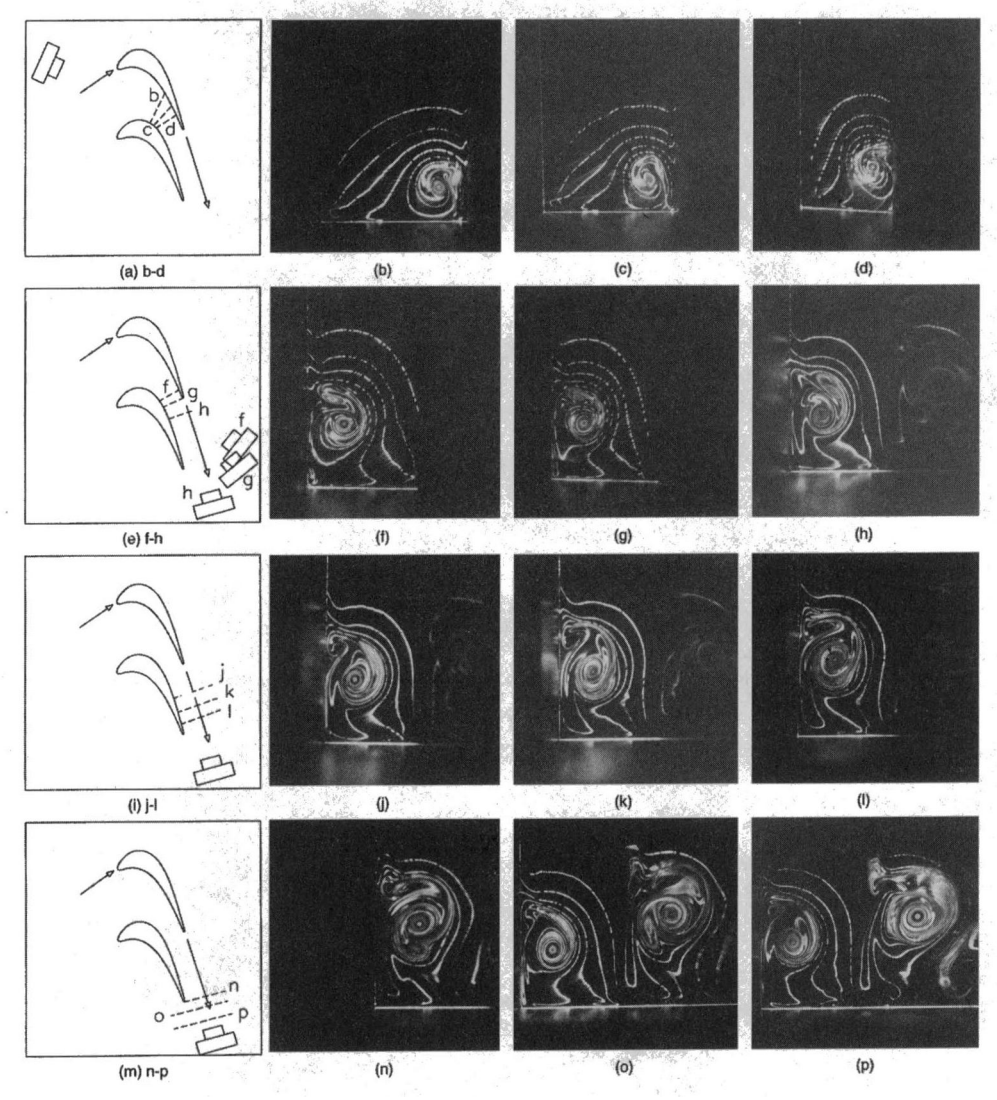


Fig. 7 Flow visualization around the blades (continued)

Passage Vortex,  $V_p$ . As mentioned above, the passage vortex consists of many flow components. The pressure leg of the horseshoe vortex is a major part of this vortex. The inlet boundary layer also contributes to it, as seen in Figs. 6(j-l). The inward rotation of the suction and pressure side legs of the horseshoe vortex system funnels part of the inlet boundary layer fluid into a smaller region, gradually extending farther above the endwall. The passage vortex stays close to the suction surface, and rotates in a counterclockwise direction when viewing the flow in the flow direction. In the geometry shown, a strong crossflow enhances its rotation and the vortex is gradually lifted away from the endwall as it travels downstream. As it entrains the main flow and endwall boundary layer, it grows in size, as shown in Fig. 7.

The mass transfer contour map from a blade near an endwall, Fig. 9 given by Goldstein et al. (1995), clearly indicates a triangular region starting near the merging point. The strong upwash motion of the passage vortex gives very high mass transfer close to the corner. The photographs also show how the incoming main flow is revolved by the passage vortex to reach the suction surface.

Suction Side Leg of the Horseshoe Vortex,  $V_{sh}$ . The multivortex suction leg quickly evolves to a single vortex as it reaches the merging point, as shown in Figs. 6(j-l). It does not move under the passage vortex, as shown in Figs. 1(a) and 1(b). The

stronger pressure side leg pulls the suction leg off the endwall. The sense of rotation of the suction side leg is clockwise when viewed in the flow direction, opposite that of the pressure side leg. As the pressure side leg of the horseshoe vortex system and the suction side leg of the horseshoe vortex system approach each other on the endwall, they constitute a counterrotating vortex pair with the suction leg being weaker (as in Fig. 6(p)).

Farther downstream, the strong rotation by the passage vortex pulls the suction leg away from the suction surface, as seen in Figs. 7(f-h). A similar pattern was also found by Sieverding and Van den Bosche (1983) and Sonoda (1985). The suction leg is wrapped around the passage vortex. This is different from the model in Fig. 1(c), which shows the suction leg moving upward on the suction surface. Nearly one revolution of the suction leg around the passage vortex has been observed at the cascade exit, which is shown in Fig. 7(n). At the exit of the cascade, the suction leg has revolved around the passage vortex and is found near the lower side of the passage vortex near the suction surface. The suction leg remains distinct as it contacts with the passage vortex and moves through the passage. To some extent, the suction leg, like the pressure leg, could be considered as a small part of the larger passage vortex system.

Wall Vortex,  $V_{wip}$ . Very close to the suction wall a small and very intense vortex is captured downstream by the camera, shown in Figs. 7(h-n). This vortex originates near the two-

6 / Vol. 119, JANUARY 1997

Transactions of the ASME

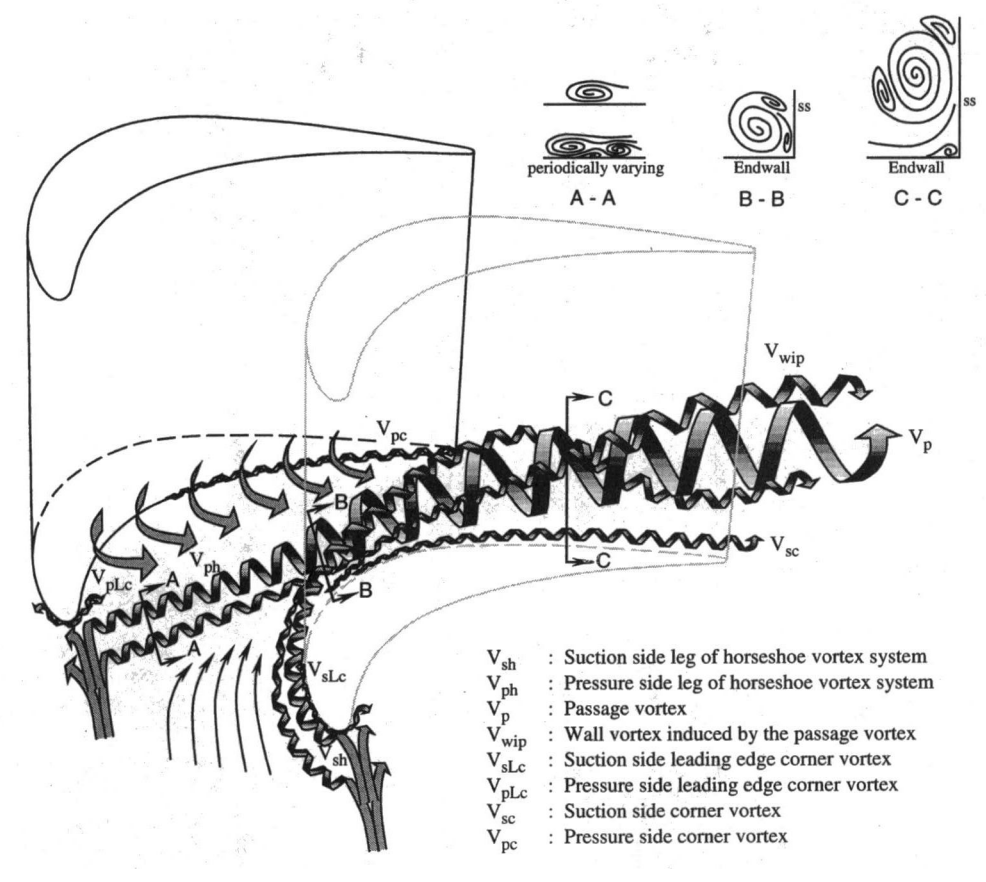


Fig. 8 Interpretation of the vortex flow pattern

leg merging point with a clockwise rotation when viewed in the flow direction and is swept up on the suction wall by the passage vortex. Jabbari et al. (1992) found in their surface flow visualization that the content of this vortex comes from the inlet boundary layer between the saddle points ahead of the cascade. Part of the boundary layer climbs on the wall and part of it stays at the suction-endwall corner. The photographs demonstrate the same flow pattern.

This new wall vortex stays above the passage vortex and counterrotates against it. Even though it has a relatively small size, it has a significant impact on mass transfer from the suction surface. Since it is so close to the wall, the upwash and downwash flows generated by this pair, passage vortex and this new wall vortex, produce a local valley and peak on the naphthalene contour map by Goldstein et al. (1995). Sonoda (1985) also found a similar phenomenon in a vane cascade.

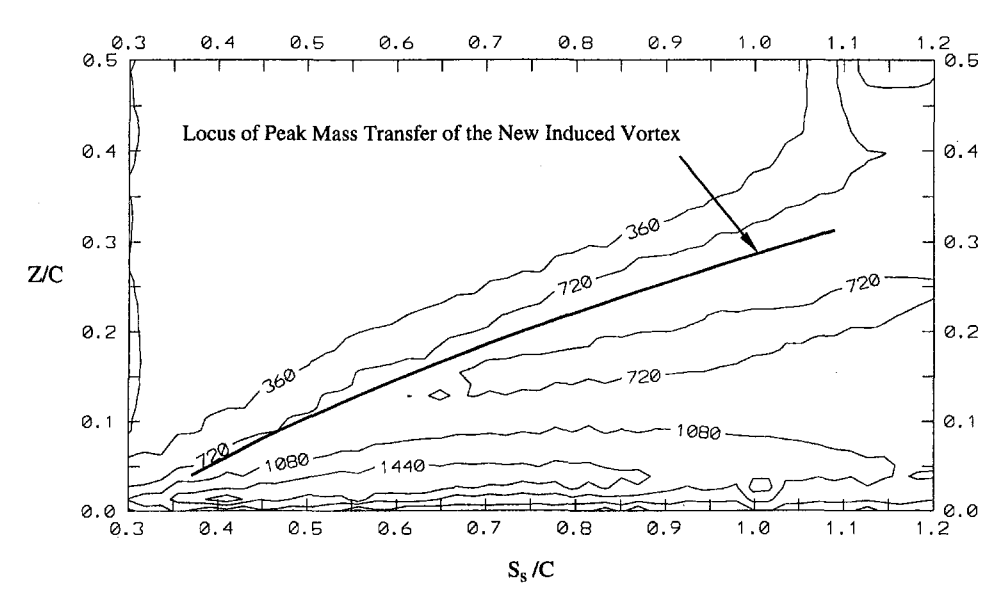


Fig. 9 Sherwood number (mass transfer) distribution on the suction side of a gas turbine blade at  $Re_{ex} = 1.73 \times 10^5$ , from Goldstein et al. (1995)

Journal of Turbomachinery

Corner Vortices,  $V_{sLc}$ ,  $V_{pLc}$ ,  $V_{sc}$  and  $V_{pc}$ . It is difficult to view a corner vortex with the smoke flow-visualization technique because of its small size. Since the corner vortex at the leading edge is driven by another larger counter-vortex around the edge, it is difficult for smoke to enter it. The surface flow visualization of Jabbari et al. (1992) and the local measurement of naphthalene mass transfer of Goldstein et al. (1995) indicate the existence of the corner vortices. Figure 8 shows the corner vortices based on the results of Jabbari et al. (1992) and Goldstein et al. (1995) although they are not clearly seen in the smoke flow visualization photographs. It is believed that the downstream corner vortex will have an impact on the corner region. These corner vortices may not be present for certain rounded corners near the leading edge.

This secondary flow pattern should be representative of other cascades, even though the leading edge radius, inlet and exit flow angle, inlet boundary layer, pitch, etc., will affect the details of the secondary flow. In particular, the multi-horseshoevortex structure formed at the leading edge may vary from cascade to cascade.

## **Conclusions**

Multiple smoke wires and a laser light sheet have been used to view the secondary flow near the endwall of a high-performance blade in a large-aspect-ratio, linear cascade. A multivortex flow pattern with periodic changing of location and number of vortices has been observed ahead of the cascade near the leading edge. Photographs and videos have been taken for archival use. A secondary flow pattern of this cascade is inferred from the flow visualization and compared with earlier mass transfer measurements. General characteristics of the flow are:

- 1 The two branches of the multiple horseshoe vortex system gradually collapse to two single vortices (a suction leg and pressure leg), which pair with oscillating motion extending downstream. The pressure leg of the horseshoe vortex travels across the passage toward the suction surface, becoming a major part of the passage vortex. It merges with the suction leg of its counterpart at about 1/4 of the surface distance from the leading edge. The passage vortex moves toward the suction side and strengthens itself by entraining the main stream flow when it flows downstream.
- 2 The suction leg of the horseshoe vortex formed ahead of the leading edge moves above the passage vortex as the pressure leg of the horseshoe vortex merges with it. It wraps itself around the passage vortex due to the strength of the passage vortex becoming a small branch of the overall passage vortex system. The crossflow does not have much effect on this leg.
- 3 A wall vortex induced by the strong passage vortex is found very close to the suction surface. It starts near the merging

point of the suction side and pressure side legs of the horseshoe vortex system and has a high mass transfer rate indicated in the naphthalene mass transfer measurement. The local minimum and peak values of the mass transfer can be explained by the upwash and downwash motions of this vortex pair.

## Acknowledgments

We would like to express our thanks to the Air Force Office of Scientific Research, and to the Advanced Turbine Systems at the Department of Energy for their support, and to project monitor Dr. Daniel Fant for his encouragement of our studies.

#### References

Chung, J. T., and Simon, T. W., 1990, "Three-Dimensional Flow Near the Blade/Endwall Junction of a Gas Turbine: Visualization in a Large-Scale Cascade Simulator," ASME Paper No. 90-WA/HT-4.

Simulator," ASME Paper No. 90-WA/HT-4.
Goldstein, R. J., and Spores, R. A., 1988, "Turbulent Transport on the Endwall in the Region Between Adjacent Turbine Blades," ASME *Journal of Heat Transfer*, Vol. 110, pp. 862–869.

Goldstein, R. J., Wang, H. P., and Jabbari, M. Y., 1995, "The Influence of Secondary Flows Near the Endwall and Boundary Layer Disturbance on Convective Transport From a Turbine Blade," ASME JOURNAL OF TURBOMACHINERY, Vol. 117, pp. 657–665.

Jabbari, M. Y., Goldstein, R. J., Marston, K. C., and Eckert, E. R. G., 1992, "Three Dimensional Flow Within Large Scale Turbine Cascades," Wärme- und Stoffübertragung, Vol. 27, pp. 51–59.

Stoffübertragung, Vol. 27, pp. 51–59.

Jilek, J., 1986, "An Experimental Investigation of the Three-Dimensional Flow Within Large Scale Turbine Cascades," ASME Paper No. 86-GT-170.

Langston, L. S., Nice, M. L., and Hopper, R. M., 1977, "Three-Dimensional Flow Within a Turbine Cascade Passage," ASME *Journal of Engineering for Power*, Vol. 99, pp. 21–28.

Langston, L. S., 1980, "Crossflows in a Turbine Cascade Passage," ASME Journal of Engineering for Power, Vol. 102, pp. 866-874.

Langston, L. S., 1990, "Research on Cascade Secondary and Tip-Leakage Flows—Periodicity and Surface Flow Visualization," *Proc. Secondary Flows in Turbomachines*, AGARD CP 469.

Marchal, P. H., and Sieverding, C. H., 1977, "Secondary Flows Within Turbomachinery Bladings," *Proc. Secondary Flows in Turbomachines*, AGARD CP 214

Moore, J., and Smith, B. L., 1984, "Flow in a Turbine Cascade: Part 2—Measurements of Flow Trajectories by Ethylene Detection," ASME *Journal of Engineering for Gas Turbines and Power*, Vol. 106, pp. 409–413.

Sharma, O. P., and Butler, T. L., 1987, "Predictions of Endwall Losses and

Sharma, O. P., and Butler, T. L., 1987, "Predictions of Endwall Losses and Secondary Flows in Axial Flow Turbine Cascades," ASME JOURNAL OF TURBO-MACHINERY, Vol. 109, pp. 229–236.

Sieverding, C. H., and Van den Bosche, P., 1983, "The Use of Coloured Smoke to Visualize Secondary Flows in a Turbine-Blade Cascade," *Journal of Fluid Mechanics*, Vol. 134, pp. 85–89.

Sieverding, C. H., 1985, "Recent Progress in the Understanding of Basic Aspects of Secondary Flows in Turbine Blade Passages," ASME *Journal of Engineering for Gas Turbines and Power*, Vol. 107, pp. 248–257.

Sonoda, T., 1985, "Experimental Investigation on Spatial Development of Streamwise Vortices in a Turbine Inlet Guide Vane Cascade," ASME Paper No. 85-GT-20.

Yamamoto, A., 1987a, "Production and Development of Secondary Flows and Losses in Two Types of Straight Turbine Cascades: Part 1—A Stator Case," ASME JOURNAL OF TURBOMACHINERY, Vol. 109, pp. 186–193.

Yamamoto, A., 1987b, "Production and Development of Secondary Flows and Losses in Two Types of Straight Turbine Cascades: Part 2—A Rotor Case," ASME JOURNAL OF TURBOMACHINERY, Vol. 109, pp. 194–200.